Structure, Martensitic Transformations, and Mechanical Properties of Aging Nanocrystalline Ti–50.9 at % Ni Alloy

T. M. Poletika[1]*****, **S. L. Girsova**[1], **S. M. Bitter**[1], **A. I. Lotkov**[1], **and K. A. Zheronkina**[2]

[1] *Institute of Strength Physics and Materials Science, Siberian Branch, Russian Academy of Sciences, Tomsk, 634055 Russia*
[2] *National Research Tomsk State University, Tomsk, 634050 Russia*
***** *e-mail: poletm@ispms.ru*

Abstract—The effect of aging temperature in the range of 300–500°C on the structure, R martensitic transformations and mechanical characteristics of nanocrystalline Ti–50.9 at % Ni alloy with a grain/subgrain structure was studied. It was found that variation in the spatial distribution of coherent Ti_3Ni_4 particles in the nanostructure from location on dislocations during low-temperature aging to precipitation at dislocation boundaries under accelerated aging is accompanied by a change in the morphology of the R phase from a nanodomain to a self-accommodating lamellar structure. The nanodomain structure of the R phase contributes to homogeneous deformation of the alloy during loading/unloading and stabilization of superelasticity. When loading the alloy with a lamellar R-phase morphology, localized deformation bands are formed by the R-phase reorientation in a Lüders deformation manner.

Keywords: nickel titanium, nanocrystalline structure, aging, coherent Ti_3Ni_4 particles, martensitic transformations, deformation, mechanical characteristics

DOI: 10.1134/S1029959924020048

1. INTRODUCTION

Alloys based on titanium nickelide have unique mechanical properties governed by the shape memory effect and superelasticity, as well as high corrosion resistance and biocompatibility [1–4], which makes them the materials of choice in medicine and technology. Of special scientific and practical interest are high-performance TiNi-based nanocrystalline alloys [5–8] processed by severe plastic deformation. In medicine, use is usually made of binary nanocrystalline TiNi alloys with a high content of Ni atoms (50.6–50.9 at %), which are prone to aging with the precipitation of coherent Ti_3Ni_4 particles and are characterized by superelasticity. In contrast to coarse-crystalline materials, the structure, martensitic transformations, and structure-sensitive properties of aging nanocrystalline TiNi alloys are understudied. They are difficult to investigate because of the need to take account of such features as the increase in the critical martensitic shear stress with grain refinement [9], multistage $B2 \leftrightarrow R \leftrightarrow B19'$ transformations [10], high density of dislocations and various boundaries after severe deformation [11], and suppression of

diffusion decomposition of B2 austenite due to the precipitation of coherent Ti_3Ni_4 particles [12]. A number of fundamental problems concerning the influence of Ti_3Ni_4 particles on the $B2 \leftrightarrow R \leftrightarrow B19'$ transformation and R-phase stabilization in nanocrystalline TiNi alloys remain unclear. The R-phase formation is usually explained by the presence of nickel-rich Ti_3Ni_4 precipitates and high internal stresses associated with coherent particles [13, 14]. Other factors promoting the $B2 \rightarrow R$ transformation in TiNi alloys include the nanocrystalline state of material [10], an increased density of defects [11], and the addition of a third element [15]. In most works, the R phase is ignored due to a small shape change (up to 1%) compared to approximately 8% during the $B2 \rightarrow B19$ transformation [16]. Very little information is available on the microscopic mechanisms of transformation and reorientation of the R phase. However, $B2 \rightarrow R$ transformations are characterized by a narrow hysteresis of phase transformation and a weak distortion of the B2 lattice. This reduces the probability of dislocation formation, thus improving the cyclic stability of the transformation and increas-

ing the fatigue strength of the material [15]. In the previous works [17, 18], we used transmission electron microscopy (TEM) to study the structure, size, and spatial distribution of coherent Ti_3Ni_4 nanoparticles in the nanocrystalline Ti−50.9 at % Ni alloy with a heterogeneous grain/subgrain structure depending on the aging temperature. The aim of the present paper is to study the influence of nanostructural evolution and coherent Ti_3Ni_4 particles with the aging temperature on martensitic transformations and mechanical properties of the nanocrystalline TiNi alloy with shape memory and superelasticity.

2. MATERIALS AND METHODS OF INVESTIGATION

The material to be studied is commercial nanocrystalline Ti–50.9 at % Ni alloy (Vascotube GmbH). Specimens had the form of tubes with the wall thickness 0.23 mm and the outer diameter 1.67 mm. Heat treatments were carried out in a salt bath for 1 h at the low-temperature aging temperatures 300 and 350°C, in the range of intense particle precipitation at 400 and 450°C [4], and at the recrystallization temperature 500°C. These aging temperatures allowed the formation of Ti_3Ni_4 particles of various sizes and morphologies. The critical temperatures of start of B2 → R martensitic transformations (T_R) and of start (M_s, A_s) and finish (M_f, A_f) of direct (M_s, M_f) and reverse (A_s, A_f) B2 ↔ B19′ martensitic transformations were determined by the electrical resistivity method (Table 1). Liquid nitrogen was used to cool specimens to cryogenic temperatures. Judging from Table 1, multistage B2 → R → B19′ transformations occur in the nanocrystalline alloy. An increase in T_R in the aging temperature range is associated with the intense precipitation of coherent Ti_3Ni_4 particles, which is accompanied by a decrease in the nickel concentration and an increase in temperature M_s [13, 14].

Table 1. Critical temperatures of direct and reverse martensitic transformations

Annealing temperature, °C	T_R, °C	A_f, °C	A_s, °C	M_s, °C	M_f, °C
Initial	7	−14	−35	−67	−134
300	34	3	−14	−42	−127
350	39	15	−7	−33	−124
400	41	27	6	−29	−78
450	29	20	3	−30	−77
500	15	10	−1	−29	−69

Uniaxial tensile tests were carried out at room temperature ($T = 20$°C) at the speed 4×10^{-5} s^{-1} on an LFM-125 testing machine (Walter + Bai AG).

Specimens were subjected to tension in the loading–unloading mode as well as to rupture. Hardened steel pins with the diameter corresponding to the inner diameter of the tube were inserted into the specimens at the sites of contact with the testing machine grips to prevent plastic deformation of the material. The following characteristics were determined: conditional yield strength $\sigma_{0.2}$, critical martensitic shear stress σ_{mt}, residual strain ε_{res}, total strain ε_{tot}, elongation to failure δ, and ultimate strength σ_B.

Microstructure of specimens was studied under a JEOL JEM 2100 transmission electron microscope. Thin foils were prepared by ion thinning on a JEOL EM 09100IS slicer. The structure of the initial specimen shown in Fig. 1a is typical for cold-deformed TiNi alloys [19]. The TiNi alloy had a heterogeneous grain-subgrain B2 austenitic nanostructure (Fig. 1a) consisting of substructural regions of submicron size (up to 800 nm) and nanograins with high-angle boundaries located predominantly within the substructural regions. The average size of nanograins/subgrains was 80 nm. Subgrains had low-angle boundaries with the azimuthal misorientation less than 3° and were characterized by a high dislocation density.

3. RESULTS AND DISCUSSION

3.1. Structure and Martensitic Transformations of the R Phase

Figure 1c shows histograms of grain/subgrain size distribution, which illustrate microstructural changes depending on the aging temperature. Thus, after low-temperature aging at 300 and 350°C, the size of nanograins/subgrains changes insignificantly, and a high density of dislocations is retained in the substructure. In the temperature range of accelerated aging (400, 450°C), the size range of polygonized nanograins/subgrains widens. A dislocation density within the subgrain structure indicates the absence of recrystallization. Recrystallization of grains/subgrains starts during 500°C annealing (Fig. 1c), resulting in the size spread of grains/subgrains and the formation of high-angle grains larger than 200 nm.

The evolution of coherent Ti_3Ni_4 particles depending on the aging temperature of the nanocrystalline TiNi alloy was previously studied [17, 18]. The following conclusions were made from the obtained data.
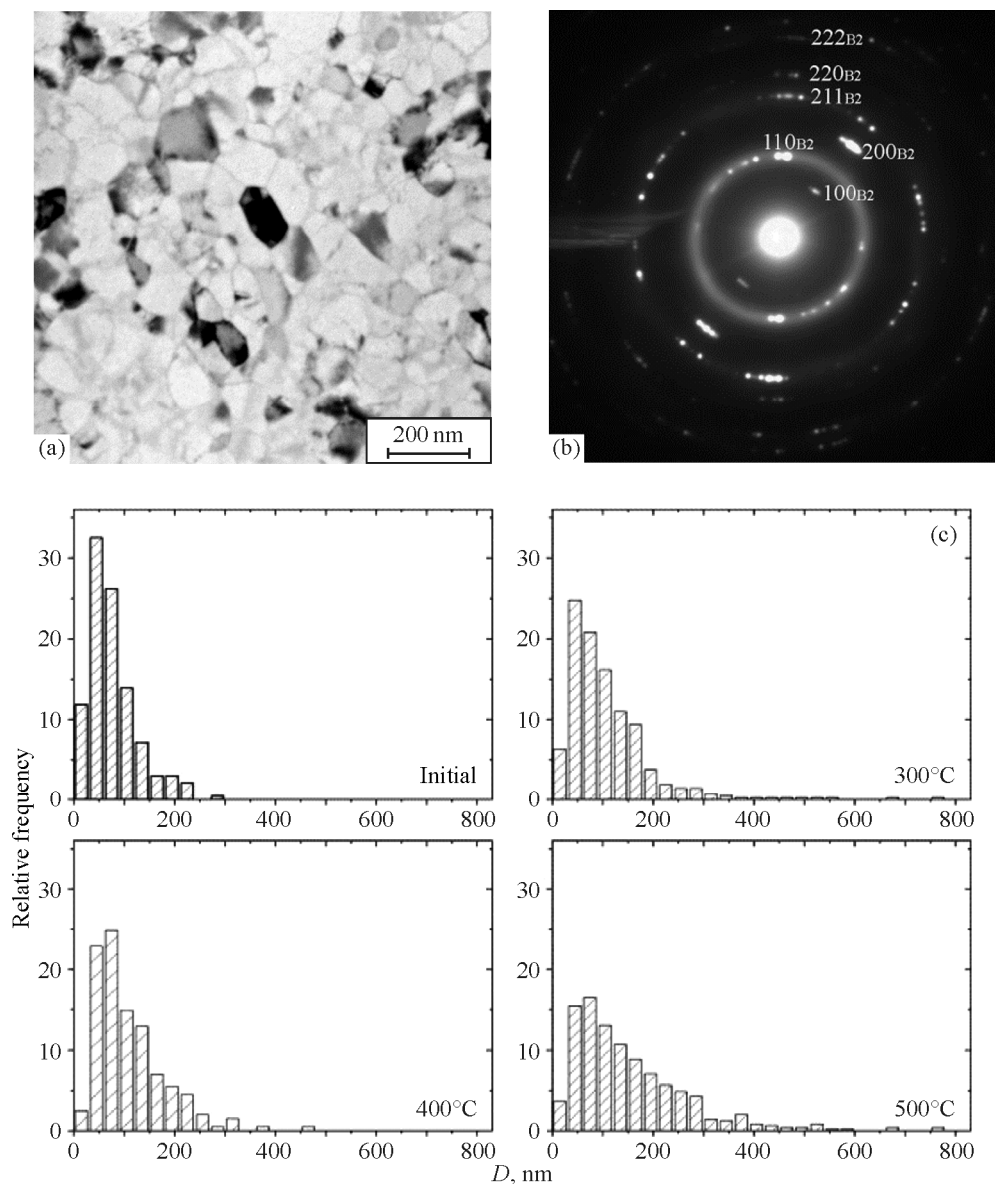
Fig. 1. Structure of the Ti–50.9 at % Ni alloy in the initial state: bright-field electron microscopic image (a) and the corresponding selected area electron diffraction (SAED) pattern (b); histograms of grain/subgrain size distribution depending on the aging temperature (c).

1. During low-temperature aging (300, 350°C), spherical coherent Ti_3Ni_4 particles up to 10 nm in size precipitate on dislocations mainly within subgrains (Fig. 2a). Ti_3Ni_4 particles are found in dislocation-containing nanograins and lack in dislocation-free nanograins. Ti_3Ni_4 precipitates are rarely observed at boundaries/subboundaries, which is associated with the low aging temperature, which does not allow Ni atoms to diffuse from the grain/subgrain interior to their boundaries.

2. In the temperature range of accelerated aging (400, 450°C) (Fig. 2b) and high diffusion activity, the

following changes occur in Ti_3Ni_4 particles: (i) their size grows (length up to 30 nm) and shape varies from spherical to lenticular; (ii) the spatial distribution changes from precipitation on dislocations to formation at low-angle boundaries. Coherent Ti_3Ni_4 particles tend to align in the {111} planes, pointing to the autocatalytic pattern of their nucleation, which is however complicated in nanograins with high-angle boundaries [13, 14].

3. Annealing at 500°C induces recrystallization of the grain/subgrain structure. It is accompanied by the dissolution of Ti_3Ni_4 particles and the growth of dis-
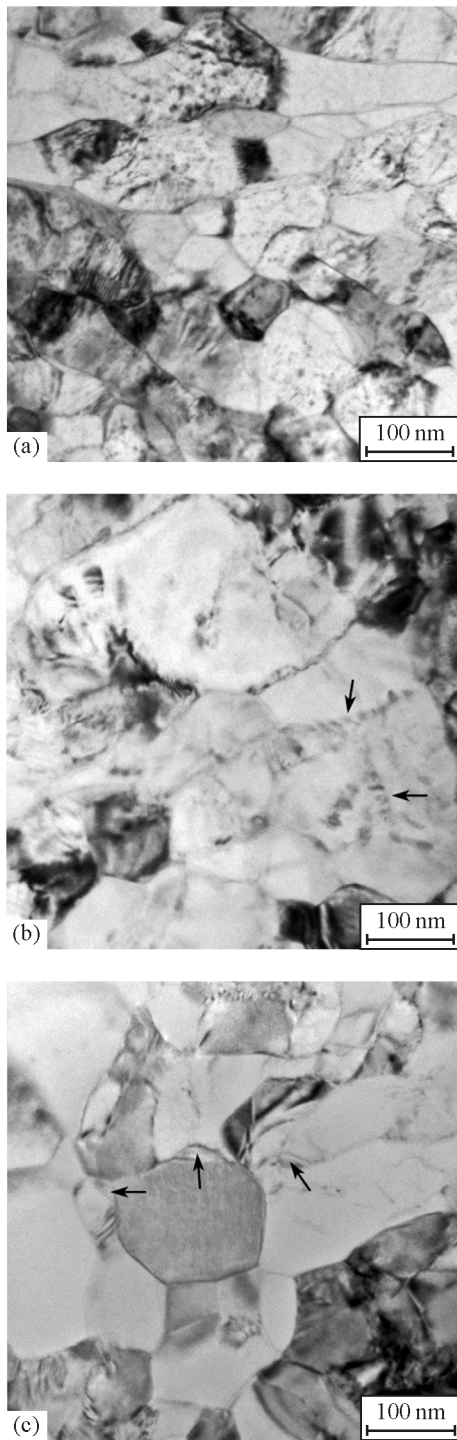
Fig. 2. Structure of the alloy after annealing at 300 (a), 400 (b), and 500°C (c). Arrows indicate aligned particles (b) and a large particle at the high-angle boundary (c) [17, 18].

location-free grains. Incoherent Ti_3Ni_4 inclusions up to 100 nm in size are formed mainly at the junctions of subgrains and at high-angle boundaries (Fig. 2c).

After annealing in the temperature range 300–450°C, the nanocrystalline Ti–50.9 at% Ni alloy is held at room temperature in the B2 + R state (Table 1). Recrystallization at 500°C and precipitation of large incoherent Ti_3Ni_4 particles lead to a decrease in T_R and the loss of the R-phase stability at the test temperature ($T = 20°C$).

It is known that the R phase in TiNi alloys nucleates around coherent Ti_3Ni_4 precipitates, which is associated with a lower Ni concentration in the interfacial region and local stress fields in the vicinity of coherent particles [13, 14, 20]. Ti_3Ni_4 particles and high dislocation density after low-temperature aging promote the nucleation and stabilization of the R phase. In this case, a complex deformation contrast is observed in bright-field TEM images of the nanostructure annealed at 300°C, which makes it difficult to identify individual Ti_3Ni_4 precipitates, R-phase crystals, and dislocations (Fig. 3a). The presence of Ti_3Ni_4 particles in the B2 matrix is evidenced by weak reflections in the selected area electron diffraction (SAED) patterns in positions 1/7 along the ⟨321⟩ reciprocal vectors of the B2 lattice (Fig. 3b). In addition, reflections of the R phase are observed in close positions 1/3 ⟨321⟩ B2 (Fig. 3b). This indicates that B2 austenite transforms into the R phase, which is stable at room temperature.

Figure 4a shows a bright-field image of the subgrain structure of the alloy aged at 300°C and the corresponding SAED pattern in the inset. Judging from the dark-field image in Fig. 4b, the R phase formed after low-temperature aging exhibits predominantly a nanodomain morphology rather than a lamellar one [21, 22]. The major cause of the formation of the nanodomain structure of the R phase in the B2 matrix of the nanocrystalline TiNi alloy is a strongly limited space of B2 → R transformations on account of a high density of defects and coherent Ti_3Ni_4 nanoparticles or atoms of the third element in nanocrystallites, which are responsible for high local stress fields [21, 22]. Nanodomains have a nearly spherical shape, measure up to 10 nm, and are located in grains/subgrains with a high density of dislocations and coherent Ti_3Ni_4 precipitates. R-phase nanodomains are uniformly distributed within the grain/subgrain structure, which is due to the uniform spatial distribution of Ti_3Ni_4 precipitates on dislocations. Groups of nanodomains have twin orientations, which is evident form the SAED pattern in the inset in Fig. 4a, where three variants of the R-phase reciprocal lattice section in the twin orientation relationship
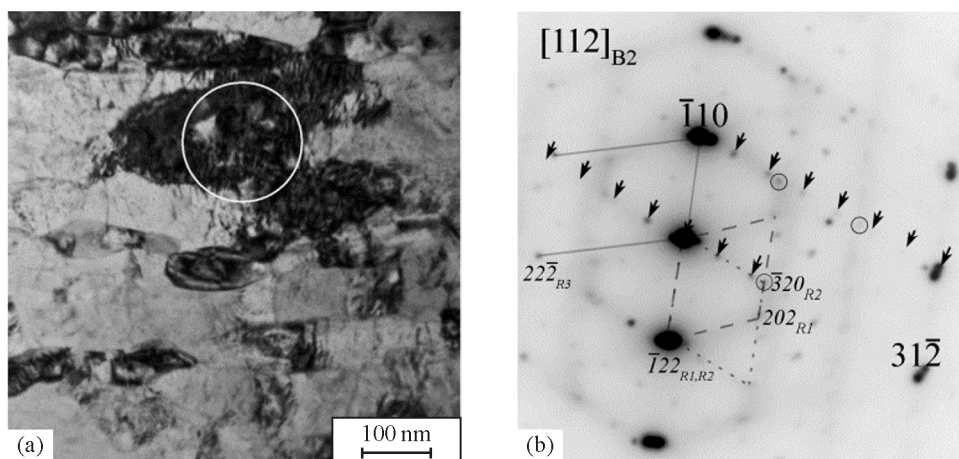
Fig. 3. Structure after annealing at 300°C: (a) bright-field electron microscopic image; (b) the corresponding SAED pattern, zone axis $Z_{B2} = [112]$, reciprocal lattice sections of the R-phase variants are marked by lines: one variant with $Z_R = [\overline{4}1\overline{3}]$ (solid line), and two variants with $Z_R = \langle 23\overline{2} \rangle$ related by the twin orientation relationship (dotted line). Arrows indicate the Ti$_3$Ni$_4$ reflections in positions $1/7\langle 321 \rangle$.
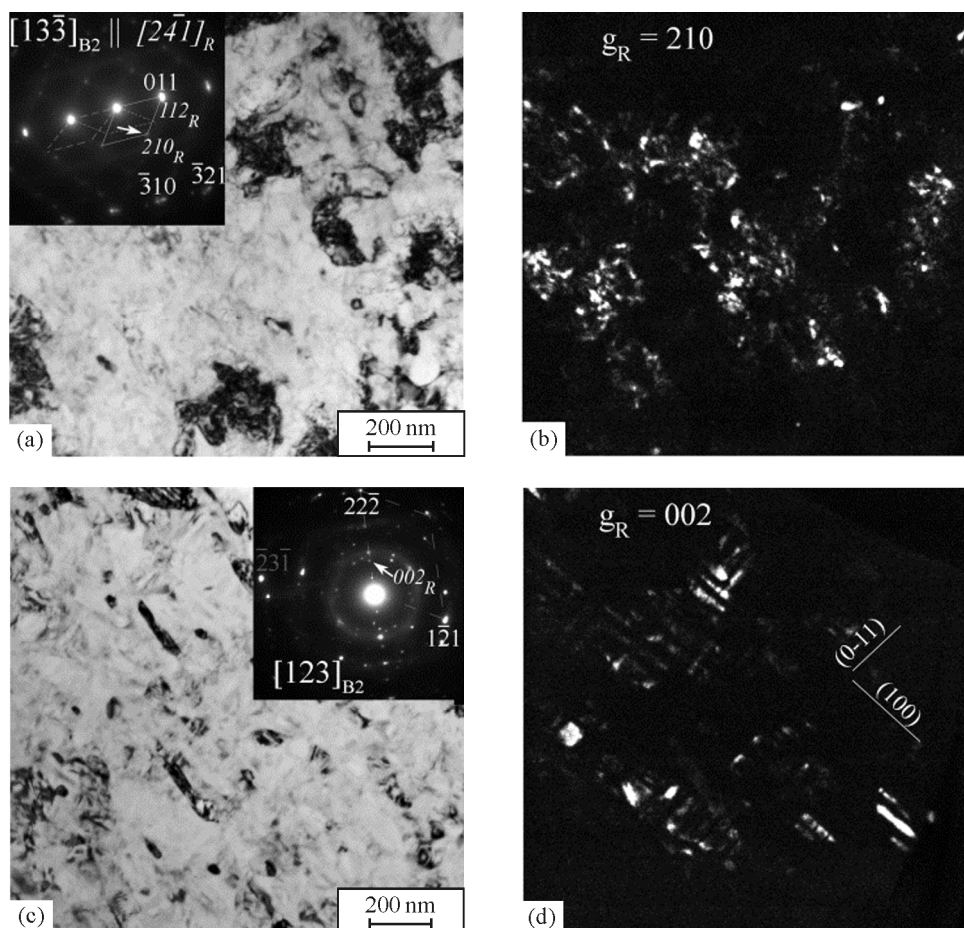

Fig. 4. Morphology of the R phase after annealing at 300 (a, b) and 450°C (c, d): (a, c) bright-field electron microscopic image and the corresponding SAED pattern, zone axes $Z_{B2} = [13\overline{3}]$ and $Z_R = [2\overline{4}1]$, the reciprocal lattice section of the R phase with $Z_R = [2\overline{4}1]$ is marked by solid lines, sections of the other two R-phase variants with $Z_R = \langle 201 \rangle$ are shown by dotted lines; (b) dark-field image of the R phase in the reflection indicated by an arrow in Fig. (a); (d) dark-field image of the R phase in the reflection indicated by an arrow in Fig. (c), plane traces corresponding to the habit planes of the R phase are shown.
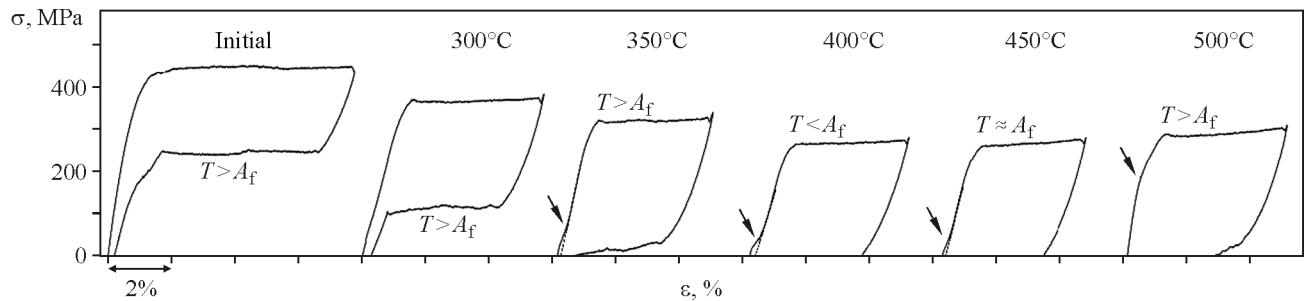
Fig. 5. Uniaxial tensile curves plotted at $T = 20°C$ in the loading–unloading mode; the arrows indicate deviation from linearity due to the stress-induced formation of the R phase.

are shown by lines (zone axis $Z_R = [2\bar{4}1]$). One to four twin variants are usually formed during the $B2 \to R$ transformation, which is associated with the mechanism of formation of the R phase by stretching the B2 lattice along four equivalent crystallographic directions $\langle 111 \rangle_{B2}$ [16, 20].

Figures 4c and 4d exhibit a typical structure of the R phase after 450°C annealing with the intense precipitation of coherent Ti_3Ni_4 particles. The observed lamellar morphology of the R phase is characteristic of R martensitic transformations in the defect-free and coarse-grained matrix. The bright-field (Fig. 4c) and dark-field images (Fig. 4d) in the SAED reflections of the R phase (inset in Fig. 4c) reveal a self-accommodating lamellar structure with the plate thickness 20–30 nm. The lamellar morphology of the R phase is observed predominantly within the substructure. In this case, plates can completely occupy both individual subgrains and their groups, which is associated with a significant decrease in the number of dislocations in subgrains and with the transfer of Ti_3Ni_4 particles from the subgrain interior to subboundaries [17, 18]. The dark-field images (Fig. 4c) show traces corresponding to the habit planes of the R phase predominantly in two orientations: $[1\bar{1}0]_{B2}$ and $[00\bar{1}]_{B2}$.

3.2. Deformation Behavior

The stress–strain curves for specimens under tension in the loading–unloading mode (Fig. 5) are typical of titanium nickelide. The first stage of the stress–strain curves is usually associated with elastic deformation of the B2 austenitic phase. All curves have a stress plateau corresponding to the initiation and propagation of macroscopic deformation bands of the Lüders type, which are caused by the $B2 \to B19'$ martensitic transformation [1, 23]. Under condition of the R-phase stability (Table 1), the alloy structure contains a mixture of the B2 + R phases, and the de-

formation behavior becomes more complex. Thus, for specimens heat treated in the range 350–450°C, the initial portion of the elastic stage slightly deviates from linearity (indicated by arrows in Fig. 5). This portion is associated with the stress-induced $B2 \to R$ transformation of the retained austenite, which is accompanied by the appearance of the final plateau corresponding to the unstable R-phase transformation [22, 24]. According to the elastic region of the deformation curve, the R phase is further deformed elastically, and possible inelastic deformation is determined by the preferred reorientation [22, 23, 25, 26], which ensures the maximum crystallographic deformation in the loading direction [23, 25]. Thus, the elastic stage of the deformation curve combines two processes: the stress-induced formation of the R phase, and the growth of the favorably oriented R phase. Figure 5 shows that these processes occur at stresses less than 100 MPa and in the strain region up to 0.2%.

The deformation curves for specimens in the initial state and after annealing at 300 and 350°C have a flag-like shape (Fig. 5), which is typical for the pseudoelastic behavior of TiNi alloys with a high nickel content at test temperatures in the range $A_f < T < T_R$ (Table 1) [1, 26]. Superelasticity is maintained by the presence of coherent Ti_3Ni_4 particles on dislocations within grains/subgrains (Fig. 2a), which lock dislocations and strengthen B2 austenite. As the aging temperature grows, irreversible strain increases up to 0.3% after 300°C annealing and up to 0.5% after 350°C annealing. A significant increase is observed in the hysteresis of the loading–unloading curves, which is mainly explained by an increase in the density of coherent Ti_3Ni_4 particles and their coarsening [1, 26].

After annealing at 400 and 450°C with the intense precipitation of Ti_3Ni_4 particles, the alloy demonstrates incomplete recovery after unloading, which may
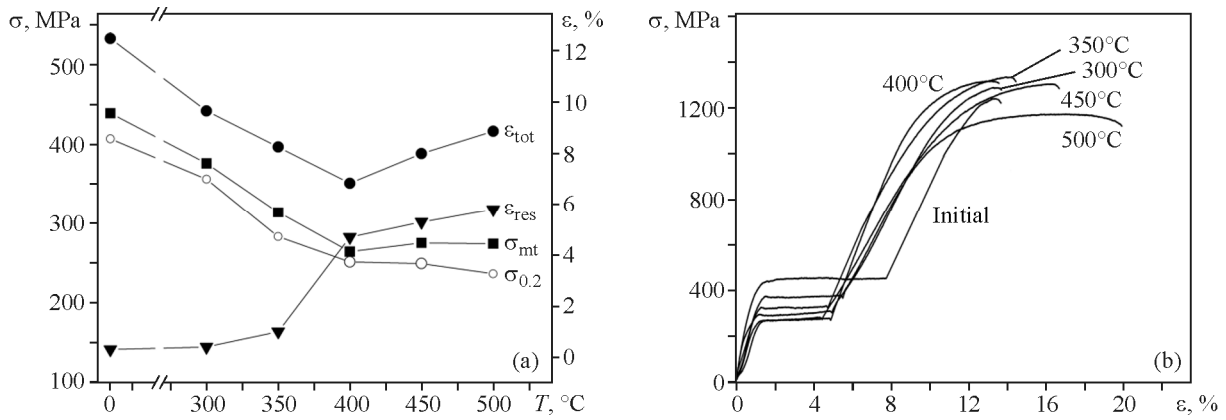
Fig. 6. Effect of the aging temperature on mechanical characteristics (a) and tensile curves for specimens in the initial state and after heat treatments (b). Test temperature $T = 20°C$.

be due to the test temperature in the range $T \leq A_f < T_R$ [1, 26].

Stages of the elastic region of the curve in Fig. 5 after 500°C recrystallization are associated with the $B2 \rightarrow R$ transformation at $A_f < T$ (indicated by an arrow) [1, 26]. The lack of recovery is a consequence of grain growth, coarsening of Ti_3Ni_4 particles, and decreased yield strength of B2 austenite. As a result, residual strain acquires a plastic component.

How mechanical characteristics of the alloy change depending on the annealing temperature is shown in Fig. 6a. It is seen that the martensitic shear stress σ_{mt} and the conditional yield strength $\sigma_{0.2}$ are maximum after low-temperature annealing at 300°C, which is associated with the suppression of the $B2 \rightarrow B19'$ martensitic transformation due to a high density of dislocations and coherent Ti_3Ni_4 nanoparticles. With increasing annealing temperature, when grains/subgrains grow in size, Ti_3Ni_4 particles coarsen and lose coherence, and the dislocation density decreases significantly, the role of local internal stresses decreases. In this case, the nickel concentration gradient becomes a governing factor, and the martensitic transformation temperature M_s increases (Table 1). In the region of the R-phase stability, stresses σ_{mt} and $\sigma_{0.2}$ decrease significantly, resulting in weakening of the material. For specimens annealed at higher temperatures (450 and 500°C), these characteristics change slightly (Fig. 6a). Moreover, in the region of the stable R phase, the plateau on the deformation curves becomes shorter (Fig. 5), which is due to a lower strain of the $R \rightarrow B19'$ transformation as compared to the $B2 \rightarrow B19'$ one [27]. As a result, the total strain ε_{tot} decreases.

Figure 6b shows examples of stress–strain curves to fracture for specimens in the initial state and after

annealing. The deformation curves of the studied specimens have almost coincident elastic stages. With further loading, the stress-induced $B2 \rightarrow B19'$ martensitic transformation occurs in the material. At higher stresses, differences are observed in the curve behavior depending on the annealing temperature. Thus, the ultimate strength σ_B changes from 1200 MPa in the initial state to 1240 MPa after 300°C annealing. A further increase in σ_B for alloys aged in the temperature range of intense precipitation of Ti_3Ni_4 particles (350–450°C) is due to additional strengthening of the material due to a high volume density of Ti_3Ni_4 particles within the grain-subgrain nanostructure. The maximum value of σ_B is achieved after annealing at 350°C, being equal to 1300 MPa. Apparently, the annealing temperature 350°C promotes an optimum combination of the size, volume fraction, and spatial distribution of highly dispersed particles within the alloy nanostructure. A further decrease in σ_B is associated with the onset of recrystallization, leading to the growth of grains/subgrains and coarsening of particles. Structural evolution of the alloy with the annealing temperature has a similar effect on relative elongation δ.

Thus, the spatial distribution of coherent Ti_3Ni_4 particles within the grain/subgrain nanostructure and its change with increasing aging temperature have a noticeable effect on martensitic transformations, the deformation behavior and mechanical characteristics of the alloy.

3.3. Alloy Structure after the Loading–Unloading Cycle

Figure 7a shows a bright-field image of the alloy aged at 300°C after the loading–unloading cycle. It is seen that the pattern of R transformations remains
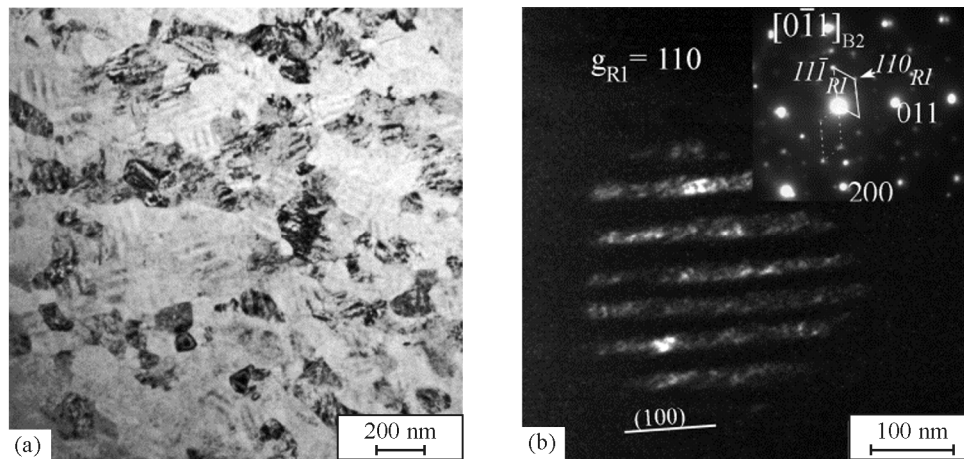
Fig. 7. Subgrain structure after annealing at 300°C: (a) bright-field electron microscopic image; (b) the corresponding SAED pattern, $Z_{B2} = [112]$, the reciprocal lattice sections of the R-phase variants are marked by lines: one variant with $Z_{R2} = [\overline{4}10]$ (solid line), and two variants with $Z_R = \langle 23\overline{2} \rangle$ related by the twin orientation relationship (dashed line). Arrows indicate the Ti_3Ni_4 reflections in positions $1/7\langle 321\rangle$.

homogeneous after unloading. The R phase forms in individual grains/subgrains and submicron conglomerates of subgrains regardless of their orientation. Figure 7b presents a dark-field image of the intragranular R phase in the $(110)_R$ reflection (SAED pattern in the inset), which reveals the internal structure of plates. Judging from the figure, the evolution of individual R-phase nanodomains during the loading–unloading cycle consists in their coalescence into 20–30-nm-wide R-phase plates, which are formed in favorable crystallographic orientations with respect to the external load (Fig. 7a). This becomes possible due to the reorientation of nanodomains within individual grains/subgrains [20, 23, 25, 26]. In this case, random local stress fields generated by defects and coherent particles stabilize the R-phase nanodomains, prevent autocatalytic processes during martensitic transformations, hinder the formation of a single-domain state during loading, and also contribute to additional restoring force during unloading [28].

A different deformation behavior is observed after the loading–unloading cycle in alloys aged at 400 and 450°C, which are characterized by a lamellar morphology of the R phase. In this case, the reorientation of R-phase plates in the subgrain structure is a cooperative process, during which local stresses in the transformed subgrain contribute to the reorientation of R plates in the neighboring subgrains [23, 25]. In Fig. 8a, subgrains with similarly oriented R plates appear in groups. Two variants of R plates are shown in the adjacent subgrains with the habit planes close to $\{100\}_{B2}$ (R1 and R2). The corresponding zones of the reciprocal lattice of the R1 and

R2 plates are shown in Fig. 8b. In the lower part of Fig. 8a, agglomerated subgrains with the habit planes close to $\{110\}_{B2}$ and $\{100\}_{B2}$ are visible. Sequential involvement of subgrains with different R plates by means of their reorientation results in large elongated regions, namely, lamellae. They contain subgrains with the most favorable orientations of R plates relative to the external load (Fig. 8c). The observed cooperative process of sequential reorientation of R plates develops in the Lüders deformation manner [20, 23, 25]. As a result, one favorable variant is formed, providing maximum crystallographic deformation in the loading direction.

In such a single-variant R state, other R variants are difficult to form, and therefore the hysteresis and residual strain increase after unloading (Figs. 5, 6). In addition, the R-phase reorientation develops at low stresses (less than 100 MPa), which is due to the presence of nanotwin boundaries between differently oriented variants [28]. It is known that nanoscale twinning effectively reduces the shear stiffness of TiNi in the martensitic state and can lead to shear instability [24, 29]. As a result, a slight reorientation can lead to strong anisotropy of the R phase even at low strain, which is retained throughout the R $\rightarrow$ B19′ transition, as well as after unloading, resulting in irreversible deformation and significant local weakening [24, 29].

Thus, the evolution of the Ti_3Ni_4 particle system with the aging temperature has a significant impact on the structure and martensitic transformations in the aging nanocrystalline TiNi alloy. The Ni concentration gradient in the B2 matrix due to Ti_3Ni_4 pre-
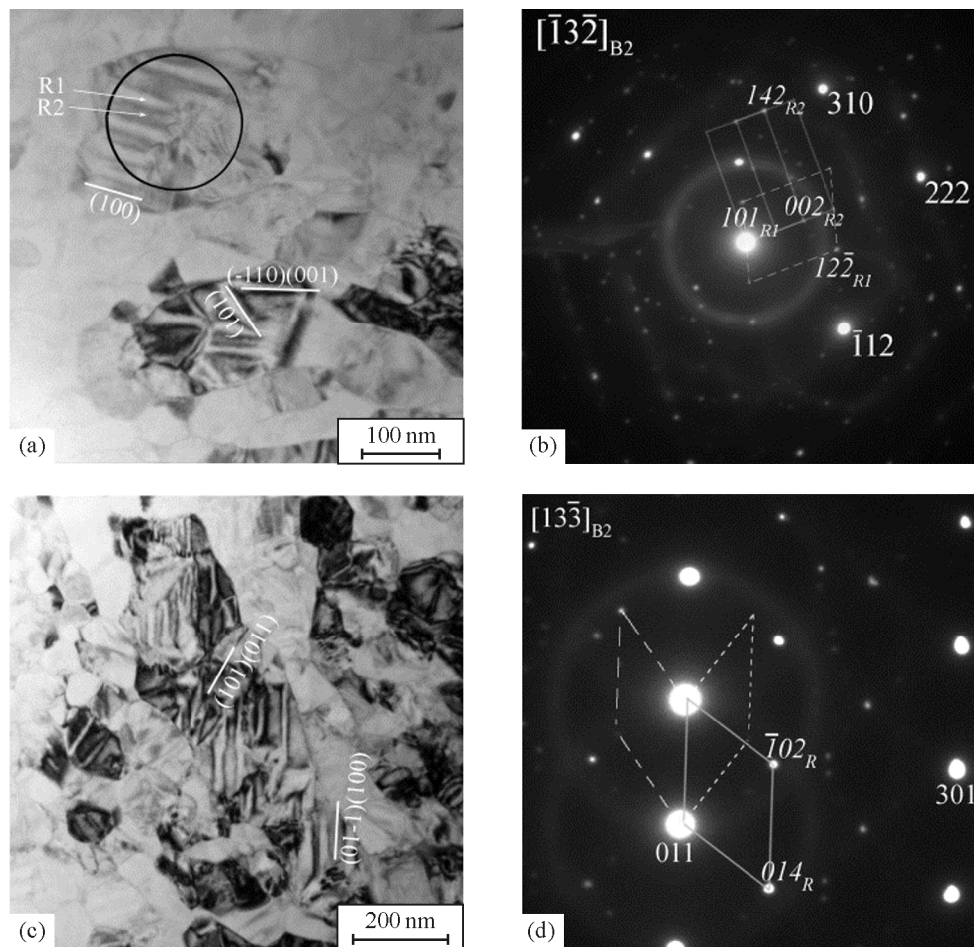
Fig. 8. Structure of specimens aged at 400°C after the loading–unloading cycle: (a, c) bright-field electron microscopic image; (b) SAED pattern of the area circled in Fig. (a), $Z_{B2} = [\bar{1}3\bar{2}]$, the R-phase reciprocal lattice sections are marked by lines: with $Z_{R2} = [\bar{4}10]$ (solid line), and with $Z_{R1} = [2\bar{3}2]$ (dotted line); (d) SAED pattern corresponding to Fig. (c), $Z_{B2} = [13\bar{3}]$, the R-phase reciprocal lattice sections are marked by lines: one variant with $Z_R = [2\bar{4}1]$ (solid line), and two variants with $Z_R = \langle 201 \rangle$ related by the twin orientation relationship (dotted line).

cipitates changes significantly the general nature of martensitic transformations, while internal stress fields formed predominantly by Ti_3Ni_4 particles play a dominant role in the morphology of R martensite. In turn, the R phase and its morphology affect the deformation behavior of nanocrystalline TiNi alloy specimens during loading–unloading and mechanical properties of the alloy.

4. CONCLUSIONS

Investigation was given to the size, shape, and spatial distribution of coherent Ti_3Ni_4 precipitates in the Ti–50.9 at % Ni alloy with a heterogeneous hierarchical grain/subgrain B2 austenitic structure after aging at the temperatures 300, 350, 400, 450, and 500°C.

A relation was found between the evolution of spatial distribution of coherent Ti_3Ni_4 particles in the grain-subgrain structure with the aging temperature of the nanocrystalline Ti–50.9 at % Ni alloy and changes in the R-phase morphology during B2 → R transformations. It was shown that, when the spatial distribution of Ti_3Ni_4 particles in the grain/subgrain structure varied from location on dislocations during low-temperature aging to precipitation at dislocation boundaries during accelerated aging, the morphology of the R phase changed from a nanodomain to a self-accommodating lamellar structure. This indicates a dominant role of internal stresses in the formation of the R-phase structure.

It was found that the nanodomain morphology of the R phase ensured homogeneous martensitic deformation and stabilization of the superelastic effect.

The alloy with a lamellar morphology of the R phase exhibited localized deformation bands formed by the R-phase reorientation in the Lüders deformation manner as well as local weakening.

The results obtained can be used for choosing heat treatment modes in the production of medical stents from nanocrystalline TiNi alloy.

FUNDING

CONFLICT OF INTEREST

The authors of this work declare that they have no conflicts of interest.

REFERENCES

1. Otsuka, K. and Ren, X., Physical Metallurgy of TiNi-Based Shape Memory Alloys, *Progr. Mater. Sci.*, 2005, vol. 50, pp. 511–678. https://doi.org/10.1016/j.pmatsci.2004.10.001

2. Elahinia, M.H., Hashemi, M., Tabesh, M., and Bhaduri, S.B., Manufacturing and Processing of NiTi Implants: A Review, *Progr. Mater. Sci.*, 2012, vol. 57, pp. 911–946. https://doi.org/10.1016/j.pmatsci.2011.11.001

3. *Shape Memory Alloys for Biomedical Applications*, Yoneyama, T. and Miyazaki, S., Eds., Cambridge: Woodhead Publishing Ltd., 2008.

4. Pelton, A.R., Russell, S.M., and DiCello, J., The Physical Metallurgy of Nitinol for Medical Applications, *JOM*, 2003, vol. 55, pp. 33–37. https://doi.org/10.1007/s11837-003-0243-3

5. Pushin, V.G., Stolyarov, V.V., Valiev, R.Z., Lowe, T.C., and Zhu, Y.T., Nanostructured TiNi-Based Shape Memory Alloys Processed by Severe Plastic Deformation, *Mater. Sci. Eng. A*, 2005, vol. 410–411, pp. 386–389.

6. Valiev, R.Z., Islamgaliev, R.K., and Alexandrov, I.V., Bulk Nanostructured Materials from Severe Plastic Deformation, *Progr. Mater. Sci.*, 2000, vol. 45, pp. 911–946. https://doi.org/10.1016/S0079-6425(99)00007-9

7. Sauvage, X., Wilde, G., Divinski, S.V., Horitac, Z., and Valiev, R.Z., Grain Boundaries in Ultrafine Grained Materials Processed by Severe Plastic Deformation and Related Phenomena, *Mater. Sci. Eng. A*, 2012, vol. 540, pp. 1–12. https://doi.org/10.1016/j.msea.2012.01.080

8. Ryklina, E.P., Polyakova, K.A., Tabachkova, N.Y., Resnina, N.N., and Prokoshkin, S.D., Effect of B2 Austenite Grain Size and Aging Time on Microstructure and Transformation Behavior of Thermomechanically Treated Titanium Nickelide, *J. Alloys Compd*, 2018, vol. 764, pp. 626–638. https://doi.org/10.1016/j.jallcom.2018.06.102

9. Waitz, T., Kazykhanov, V., and Karnthaler, H.P., Martensitic Phase Transformations in Nanocrystalline NiTi Studied by TEM, *Acta Mater.*, 2004, vol. 52, pp. 137–147. https://doi.org/10.1016/j.actamat.2003.08.036

10. Shi, X., Cui, L., Jiang, D., Yu, C., Guo, F., Yu, M., Ren, Y., and Liu, Y., Grain Size Effect on the R Phase Transformation of Nanocrystalline NiTi Shape Memory Alloys, *J. Mater. Sci.*, 2014, vol. 49, pp. 4643–4647. https://doi.org/10.1007/s10853-014-8167-6

11. Mahmud, A.S., Wu, Z., Yang, H., and Liu, Y., Effect of Cold Work and Partial Annealing on Thermomechanical Behaviour of Ti–50.5 at % Ni, *Shape Mem. Superelasticity*, 2017, vol. 3, pp. 57–66. https://doi.org/10.1007/s40830-017-0103-6

12. Prokofiev, E.A., Burow, A., Payton, E., Zarnetta, R., Frenzel, J., Gunderov, D., Valiev, R., and Eggeler, G., Suppression of Ni_4Ti_3 Precipitation by Grain Size Refinement in Ni-Rich NiTi Shape Memory Alloys, *Adv. Eng. Mater.*, 2010, vol. 12, p. 747. https://doi.org/10.1002/adem.201000101

13. Khalil-Allafi, J., Dlouhý, A., and Eggeler, G., Ni_4Ti_3-Precipitation during Aging of NiTi Shape Memory Alloys and Its Influence on Martensitic Phase Transformations, *Acta Mater.*, 2002, vol. 50, pp. 4255–4274. https://doi.org/10.1016/S1359-6454(02)00257-4

14. Zheng, Y., Jiang, F., Li, L., Yang, H., and Liu, Y., Effect of Ageing Treatment on the Transformation Behaviour of Ti–50.9 at % Ni Alloy, *Acta Mater.*, 2010, vol. 58, pp. 3444–3458. https://doi.org/10.1016/j.actamat.2007.10.020

15. Chen, Y., Li, A., Ma, Z., Wang, T., Liu, Y., Yu, K., Yang, F., Jiang, D., Zhao, K., Yang, H., Ren, Y., and Cui, L., Step-Wise R Phase Transformation Rendering High-Stability Two-Way Shape Memory Effect of a NiTiFe-Nb Nanowire Composite, *Acta Mater.*, 2021, vol. 219, p. 117258. https://doi.org/10.1016/j.actamat.2021.117258

16. Wang, X.B., Verlinden, B., and Van Humbeeck, J., R-Phase Transformation in NiTi Alloys, *Mater. Sci. Technol.*, 2014, vol. 30, pp. 1517–1529. https://doi.org/10.1179/1743284714Y.0000000590

17. Poletika, T.M., Girsova, S.L., and Lotkov, A.I., Ti_3Ni_4 Precipitation Features in Heat-Treated Grain/Subgrain Nanostructure in Ni-Rich TiNi Alloy, *Intermetallics*, 2020, vol. 127, p. 106966. https://doi.org/10.1016/j.intermet.2020.106966

18. Poletika, T.M., Girsova, S.L., Lotkov, A.I., Kudryachov, A.N., and Girsova, N.V., Structure and Multistage Martensite Transformation in Nanocrystalline Ti-50.9Ni Alloy, *Metals*, 2021, vol. 11, p. 1262. https://doi.org/10.3390/met11081262

19. Prokoshkin, S., Dubinskiy, S., and Brailovski, V., Features of a Nanosubgrained Structure in Deformed and

Annealed Ti-Ni SMA: A Brief Review, *Shap. Mem. Superelasticity*, 2019, vol. 5, pp. 336–345. https://doi.org/10.1007/s40830-019-00241-6

20. Miyazaki, S. and Wayman, C.M., The R-Phase Transition and Associated Shape Memory Mechanism in Ti-Ni Single Crystals, *Acta Metall.*, 1988, vol. 36, pp. 181–192.

21. Chen, Y., Liu, Y., Yu, K., Yang, F., Jiang, D., Ren, Y., and Cui, L., Small-Scale Confined R-Phase Transformation in $Ni_{47}Ti_{49}Fe_2Nb_2$ Alloy, *Materialia*, 2021, vol. 20, p. 101262. https://doi.org/10.1016/j.mtla.2021.10126

22. Wang, D., Hou, S., Wang, Yu, Ding, X., Ren, S., Ren, X., and Wang, Y., Superelasticity of Slim Hysteresis over a Wide Temperature Range by Nanodomains of Martensite, *Acta Mater.*, 2014, vol. 66, pp. 349–359. https://doi.org/10.1016/j.actamat.2013.11.022

23. Šittner, P., Landa, M., Lukáš, P., and Novák, V., R-Phase Transformation in NiTi Alloys, *Mech. Mater.*, 2006, vol. 38, pp. 475–492. https://doi.org/10.1016/j.mechmat.2005.05.025

24. Favier, D., Louche, H., Schlosser, P., Orgéas, L., Vacher, P., and Debove, L., Homogeneous and Heterogeneous Deformation Mechanisms in an Austenitic Polycrystalline Ti–50.8 at % Ni Thin Tube under Tension. Investigation Via Temperature and Strain Fields Measurements, *Acta Mater.*, 2007, vol. 55, pp. 5310–5322. https://doi.org/10.1016/j.actamat.2007.05.027

25. Feng, B., Kong, X., Hao, S., Liu, Y., Yang, Y., Yang, H., Guo, F., Jiang, D., Wang, T., Ren, Y., and Cui, L., In-Situ Synchrotron High Energy X-Ray Diffraction Study of Micromechanical Behaviour of R Phase Reorientation in Nanocrystalline NiTi Alloy, *Acta Mater.*, 2020, vol. 194, pp. 565–576. https://doi.org/10.1016/j.actamat.2020.05.004

26. Miyazaxi, S. and Otsuka, K., Deformation and Transition Behavior Associated with the R-Phase in Ti-Ni Alloys, *Metall. Mater. Trans. A*, 1986, vol. 17, pp. 53–63. https://doi.org/10.1007/BF02644442

27. Zhang, X. and Sehitoglu, H., Crystallography of the $B2 \rightarrow R \rightarrow B19$ Phase Transformations in NiTi, *Mater. Sci. Eng. A*, 2004, vol. 374, pp. 292–302. https://doi.org/10.1016/j.msea.2004.03.013

28. Wang, D., Hou, S., Wang, Yu., Ding, X., Ren, S., Ren, X., and Wang, Y., Superelasticity of Slim Hysteresis over a Wide Temperature Range by Nanodomains of Martensite, *Acta Mater.*, 2014, vol. 66, pp. 349–359. http://dx.doi.org/10.1016/j.actamat.2013.11.022

29. Wang, J. and Sehitoglu, H., Martensite Modulus Dilemma in Monoclinic NiTi—Theory and Experiments, *Int. J. Plast.*, 2014, vol. 61, pp. 17–31. https://doi.org/10.1016/j.ijplas.2014.05.005